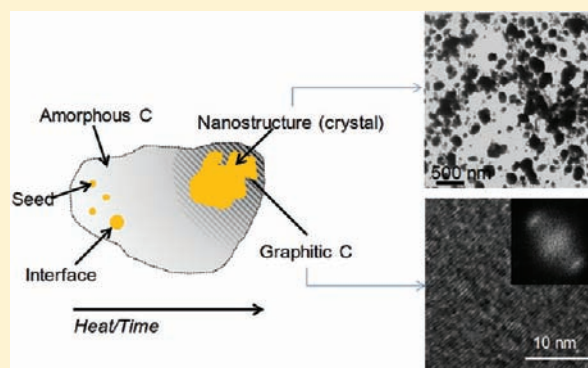


## Layered Graphitic Carbon Host Formation during Liquid-free Solid State Growth of Metal Pyrophosphates

Carlos Díaz,<sup>\*,†</sup> María Luisa Valenzuela,<sup>‡</sup> Vladimir Lavayen,<sup>§</sup> and Colm O'Dwyer<sup>\*,†,||,⊗</sup><sup>†</sup>Department of Chemistry, Faculty of Science, Universidad of Chile, Casilla 653, Santiago, Chile<sup>‡</sup>Departamento de Ciencias Químicas, Facultad de Ciencias Exactas, Universidad Andres Bello, Av. Republica 275, Santiago, Chile<sup>§</sup>Faculdade de Química, Pontificia Universidade Católica do Rio Grande do Sul, Porto Alegre-RS CEP 90619-900, Brazil<sup>||</sup>Department of Physics and Energy and <sup>⊗</sup>Materials and Surface Science Institute, University of Limerick, Limerick, Ireland

**ABSTRACT:** We report a successful ligand- and liquid-free solid state route to form metal pyrophosphates within a layered graphitic carbon matrix through a single step approach involving pyrolysis of previously synthesized organometallic derivatives of a cyclo-triphosphazene. In this case, we show how single crystal  $Mn_2P_2O_7$  can be formed on either the micro- or the nanoscale in the complete absence of solvents or solutions by an efficient combustion process using rationally designed macromolecular trimer precursors, and present evidence and a mechanism for layered graphite host formation. Using in situ Raman spectroscopy, infrared spectroscopy, X-ray diffraction, high resolution electron microscopy, thermogravimetric and differential scanning calorimetric analysis, and near-edge X-ray absorption fine structure examination, we monitor the formation process of a layered, graphitic carbon in the matrix.

The identification of thermally and electrically conductive graphitic carbon host formation is important for the further development of this general ligand-free synthetic approach for inorganic nanocrystal growth in the solid state, and can be extended to form a range of transition metals pyrophosphates. For important energy storage applications, the method gives the ability to form oxide and (pyro)phosphates within a conductive, intercalation possible, graphitic carbon as host-guest composites directly on substrates for high rate Li-ion battery and emerging alternative positive electrode materials.



## 1. INTRODUCTION

Graphitic carbonaceous materials, including nanohorns, nanorods, nanofibers, nanocages, and of course nanotubes,<sup>1</sup> fullerenes, and graphene<sup>2</sup> have a number of definitive uses including their application in electrical and thermal devices, as adsorbent, sieving, and storage media including  $H_2$  storage, and as catalytic supports, because of their unique chemical and physical properties.<sup>3–5</sup> The recent development of graphitic foams<sup>6</sup> characterized by highly aligned graphitic structures has attracted attention for thermal management devices,<sup>7</sup> and with unusually high thermal conductivity-to-weight ratios such graphitic carbons are promising aeronautical and aerospace industrial materials. Among the many methods for carbon nanostructure growth,<sup>8–10</sup> the organometallic approach<sup>11–13</sup> has been widely used and is one of the principal synthetic methods. The organometallic compound involves the pyrolysis of the precursors at elevated temperatures under a  $N_2$  atmosphere or vacuum.<sup>12</sup> Typically, the metal catalyzes the transformation of the organic matter to graphitic materials. Cage-like carbons, for example, have been fabricated by a template method where carbon shells encapsulated with Fe particles were first generated by laser-induction complex heating evaporation, followed by removal of the catalyst with an inorganic acid.<sup>14</sup> Such carbons are analogous to cyclo-

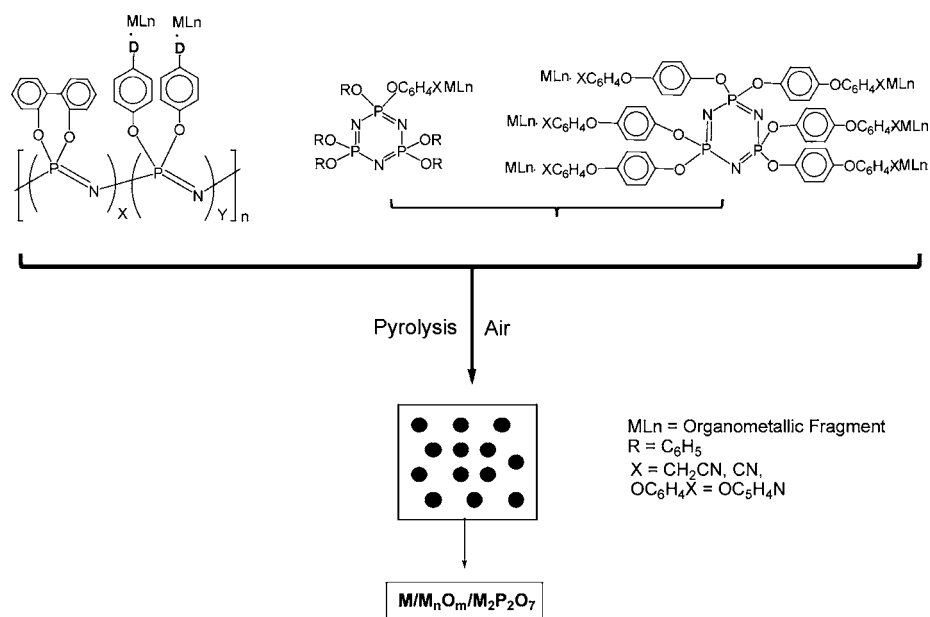
matrixes formed during thermolysis of carbon containing liquids, solvents, and polymers.

While the plethora of carbon and graphitic nanostructures owe their synthetic origins to many metallic catalysts and associated reactions, carbons can also influence the growth of metallic structures. There are many known methods for preparing metallic nanostructures, and solution-based methods have been the most prevalent, owing to the relatively simple chemistries involved in reducing metallic salts in appropriate solvents.<sup>15–17</sup> By comparison, relatively few solid-state strategies for pure metallic nanostructured materials have been reported.<sup>18–22</sup> In recent work,<sup>23–29</sup> we reported a new solid-state method allowing the formation of metallic (M), oxidic ( $M_xO_y$ ), and (pyro)phosphate-based ( $M_xP_yO_z$ ) nanostructured materials without necessitating liquids or solutions. Detailed investigations have shown that the resulting structures and their shapes strongly depend on the metal used, which can be a noble, transition, or valve metal, and also on the molecular precursors to which the metal centers are coordinated. The strategy involves the design and pyrolysis of organometallic derivatives of poly- and cyclo-triphosphazenes with coordinated

Received: February 27, 2012

Published: May 15, 2012

**Scheme 1. Schematic Representation of the Solid-State Method for the Synthesis of Nanostructured Materials from Oligomeric and Polymeric Precursors**



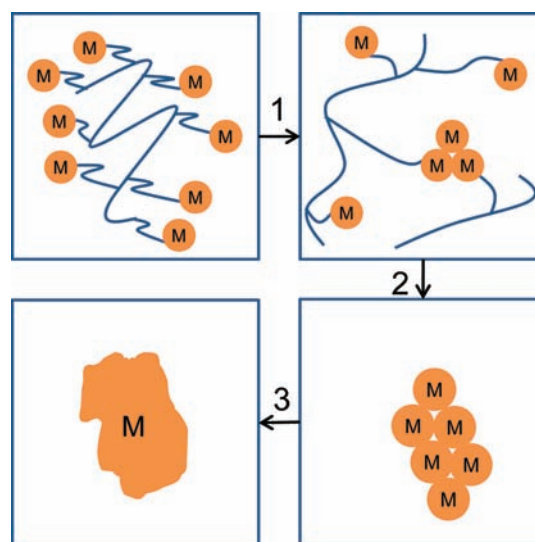
metals that allows the formation of the resulting metallic nanomaterials, as summarized in Scheme 1 below.

Another aspect of this approach is that the composition and the morphology of the pyrolytic products are also sensitively dependent on the structure of the organometallic precursors. Because of this overarching dependence, and the fact that a wide range of materials and shapes are possible through precursor design, information is needed on the complex thermal decomposition processes as a function of the precursor structure and its resulting influence on the growth of the inorganic phase. Here, we explore the general mechanism for this overall solid state strategy and specifically detail the formation and mechanism of layered graphitic carbon formation inside which the crystalline nanomaterials are formed. The mechanism of formation of nanoparticles in solution is now very well advanced,<sup>30–35</sup> and significant insight into the solid state precursor-mediated method can be extracted from the formation of these nanomaterials, including the influence of the host matrix on the crystal growth of the noncarbonaceous phase. This was recently demonstrated by Tannenbaum et al.<sup>35</sup> in the solid state preparation of metallic nanoparticles embedded in polymer. More recently, the pyrophosphates and phosphates which can result from the precursors by our method have been investigated within the past year<sup>36</sup> as useful Li-ion battery materials, and this approach augurs well for the creation of a wide variety of transition metal-based pyrophosphates as tunnel-structure intercalation hosts for battery materials and energy storage. Conductive layered, conductive graphitic carbon additives are formed in intimate contact with intercalation-possible inorganic (pyro)phosphate and oxide crystals directly on substrates, a one-step battery composite material without any liquid-based synthetic steps.

For the solid state method outlined in Scheme 1, we have proposed a mechanism principally based on thermogravimetric (TG) and differential scanning calorimetric (DSC) studies of precursor pyrolysis. This mechanism is outlined in Scheme 2.

The first step involves the cross-linking of the polymer chains or the trimer to create a three-dimensional (3-D) network or

**Scheme 2. Schematic Representation of the Proposed Solid State Mechanism of Nanoparticle Formation<sup>a</sup>**

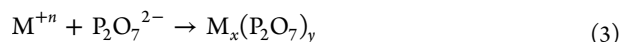


<sup>a</sup>Continual polymeric or trimeric decomposition occurs during pyrolysis resulting in crystals aggregation and ripening of cleaved metallic centers in a graphitizing carbon matrix.

matrix. As previously shown,<sup>24</sup> this step is essential in preventing the volatilization of the sample on heating. The second step involves carbonization of the organic matter. This step produces the CO/CO<sub>2</sub> mixtures; these gaseous products form holes in a thermally decomposing polymer and allow the agglomeration of cleaved metallic centers from the precursor to ripen into metallic nanoparticles. The formation of metal oxide nanoparticles can then occur in two steps: (1) Oxidation of the previously formed metal with a neutral oxidation state, which can occur in the presence of O<sub>2</sub> from reduction of CO/CO<sub>2</sub> mixtures and the corresponding M<sup>0</sup> ion, and (2) direct reaction of the M<sup>+n</sup> ion (*n* = valence state) with O<sub>2</sub>:



On the other hand, metal pyrophosphate nanostructured salts can be formed by simple reaction of the  $M^{+n}$  ions (as in the case of Mn in Scheme 1) with the in situ formed pyrophosphate anions from oxidation of the phosphazene P atoms:



In all cases a low metal/P,N ratio produces  $P_4O_7$  or  $P_4O_9$  molecules in excess which act as a stabilizing matrix for the nanoparticles. The step involving the carbonization of the organic matter is expected to form some carbonaceous material, at intermediate temperatures. To investigate the composition and structure of the important carbon host matrix, we report detailed in situ heated Raman scattering, FTIR, SEM-EDAX, HRTEM and TG/DSC studies of the solid-state pyrolysis of trimer (1), reproduced in Figure 1 below, and we show that the

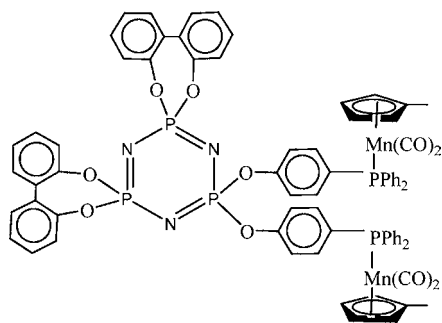


**Figure 1.** Schematic representation of  $\{NP(OC_8H_{12})_2(OC_6H_4PPh_2-Mn(CO)_2(\eta^5-C_5H_4Me)_2)\}_3$  (1).

pyrolytic decomposition mechanism of the precursor results in a layered, graphitic carbon matrix where metal, metal oxide, and metal pyrophosphate nanostructures can form, and this work shows that it is mediated by the conversion of an initially amorphous matrix to polycrystalline graphitic carbon. The findings are generally applicable to the many solid state precursors so far investigated.

## 2. EXPERIMENTAL SECTION

**2.1. Precursor.** The compound  $\{NP(OC_8H_{12})_2(OC_6H_4PPh_2-Mn(CO)_2(\eta^5-C_5H_4Me)_2)\}_3$  (1) was prepared as previously reported.<sup>37</sup>

**2.2. Pyrolysis.** The pyrolysis experiments were made by pouring a weighed portion (0.05–0.15 g) of the precursor trimer (1) into aluminum oxide boats that were placed in a furnace (Daihan oven model Wise Therm FHP-12) under a flow of air, heating from 25 °C to upper temperature limits of 250, 300, 315, 325, 400, 600, and 800 °C, followed by annealing for 2 h in each case. The heating rate was consistently maintained at 10 °C min<sup>-1</sup> for all experiments.

**2.3. Characterization of the Pyrolytic Samples.** Solid pyrolytic samples were characterized by scanning electron microscopy (SEM), high resolution transmission electron microscopy (HRTEM), Fourier transform infrared (FTIR) spectroscopy, Raman scattering spectroscopy and thermogravimetric (TG) and differential scanning calorimetric (DSC) analysis. SEM images were acquired with a Philips EM 300 scanning electron microscope. Energy dispersive X-ray analysis (EDAX) was performed on a NORAN Instrument microprobe attached to a JEOL 5410 scanning electron microscope. TEM data were acquired using a JEOL SX100 and a JEOL 2011 transmission electron microscope. The TEM samples were prepared by dispersing pyrolyzed material onto copper grids and dried at room

temperature. For high resolution examination of graphitic carbons, flakes of sonicated carbons were dispersed on grids and examined under SEM to determine their thickness. Graphitic samples were left intentionally >100 nm thick to compensate for beam damage to the exposed surface.

X-ray diffraction (XRD) was conducted at room temperature on a Siemens D-5000 diffractometer with  $\theta$ - $2\theta$  geometry. The XRD data was collected using Cu-K $\alpha$  radiation (40 kV, 30 mA). FTIR measurements were performed on a Perkin-Elmer FTIR spectrophotometer model Spectrum BXII. Raman scattering measurements were performed on a Renishaw Raman Microscope System RM1000 equipped with a 2.41 eV laser line. The output laser power was maintained in the range 10–100 mW, resulting in maximum laser power densities <10<sup>7</sup> W cm<sup>-2</sup>.

TGA and DSC measurements were performed on a Mettler TA 4000 instrument and Mettler DSC 300 differential scanning calorimeter, respectively. The trimer samples were heated at a rate of 10 °C min<sup>-1</sup> from ambient temperature to 1000 °C under a constant flow of nitrogen.

Near-edge X-ray absorption fine structure (NEXAFS) measurements were carried out at the PM-3 beamline of the BESSY Synchrotron Radiation Facility in Berlin, Germany. Thin film deposits of the carbon material pyrolyzed to 800 °C were examined on metallized silicon substrates. NEXAFS spectra at the carbon and oxygen K-edges were measured. Data were captured with surface sensitive total electron yield at an angle of incidence of 45° and were normalized to data of the metallized substrate.

## 3. RESULTS AND DISCUSSION

**3.1. Crystal Growth during Initial Pyrolysis.** Pyrolysis of the complex precursor (1) under air and at 800 °C results in a white solid identified by powder XRD, shown in Figure 2a, as  $Mn_2P_2O_7$  (ICDD File No. 29-0891). Similar single crystal pyrolytic products were obtained from the pyrolysis of the trimer compound  $\{NP(OC_6H_4PPh_2-Mn(CO)_2(\eta^5-C_5H_4Me)_2)\}_3$  as well as from the analogous polymer<sup>38</sup> and related systems. The material is a porous solid; the solid regions comprise the

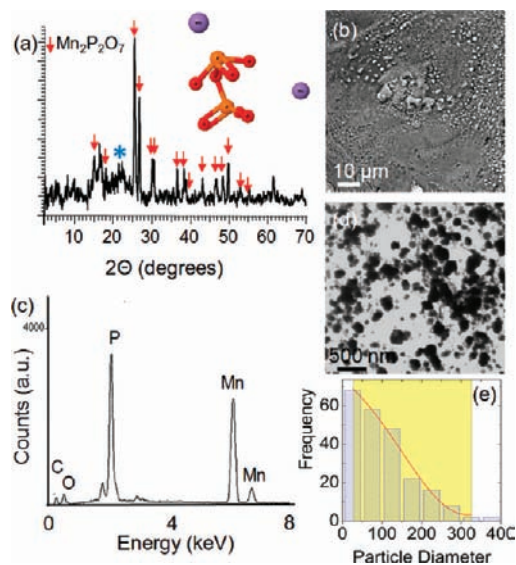


**Figure 2.** (a) X-ray diffraction analysis of the  $Mn_2P_2O_7$  (ICDD, No. 29-0891) crystalline product from pyrolysis of  $NP(OC_8H_{12})_2(OC_6H_4PPh_2-Mn(CO)_2(\eta^5-C_5H_4Me)_2)_3$ . Arrows highlight  $Mn_2P_2O_7$  peaks and \* marks the (002) diffraction from graphite. (b) Corresponding survey scanning electron microscopy image of the pyrolytic product. (c) Energy dispersive X-ray analysis of the products confirming the presence of Mn, P, O, and C. (d) TEM analysis of crystalline particles and (e) corresponding particle size distribution.

pyrolyzed single crystal materials interspersed with voids or pores akin to disordered mesoporous materials. Accounting for known size distributions in the Scherrer constant or by estimating variances from a unimodal distribution using Warren-Averbach approaches to the Fourier transform of XRD data does not confirm the size distribution, and the best estimates are found from large area TEM images acquired at high angle to maximize contrast from the higher scattering  $\text{Mn}_2\text{P}_2\text{O}_7$  (compared to carbon). The XRD pattern in Figure 2a also displays a broad peak centered at approximately  $26^\circ 2\theta$ , from the (002) reflection of graphite with a corresponding spacing between planes of carbon of  $\sim 0.34$  nm. The appearance of this broad peak indicates that the initial amorphous structure of the carbonized organic matter becomes more ordered during intermediate pyrolysis temperatures as the carbon converts to graphitic carbon.

The morphology of the product is that of a porous matrix that contains the  $\text{Mn}_2\text{P}_2\text{O}_7$  crystals, as is shown in Figure 2b. EDAX analysis (Figure 2c) confirms the presence of mainly Mn, P, C, and O. As this material is analyzed after full pyrolysis and annealing at  $800^\circ\text{C}$ , the resulting quantity of carbon is quite small compared to intermediate stages, shown further on. TEM analysis of some of the crystalline material shows that it is primarily composed of irregular crystals with a broad size distribution as shown in Figure 2d. Particles with sizes in the range 200–450 nm are typically observed, confirming global estimates from XRD data. The size distribution in Figure 2e confirms a log-normal variation of particle sizes, accounting for asphericity in microscopy images.

**3.2. Raman Scattering and Vibrational Spectroscopy of Decomposition and Graphitization.** Since the formation of the nanoparticles and crystals depends on several key steps such as (1) the thermal dewetting characteristics of the solidifying polymer and its influence on nanoscale seed particle coarsening by solid stage diffusion barriers, (2) cleavage of metal centers so that aggregation occurs to seed metallic crystals (and subsequent oxidation for oxides), which incubate in the porous carbonizing host, and (3) the composition and crystallinity of the matrix in which the particles grow, we investigated the intermediate temperatures during pyrolysis to clarify the matrix structure and composition. For nanoparticles to form, it is known that carbonaceous matrixes require higher temperatures than oxides for metallic nanoparticle seed ripening to occur, owing to the high thermal conductivity of the carbon.<sup>39,40</sup> Using IR absorbance, we monitored the molecular vibrations of the  $\nu\text{CO}$  region of the cymantrene<sup>39</sup> groups of precursor (1) during pyrolytic annealing at several temperatures, shown in Figure 3. On heating from 250 to  $400^\circ\text{C}$ , we observe the complete disappearance of the  $\nu\text{CO}$  bands from the cymantrene groups. The progressive decrease of the two absorption bands of the  $\text{Mn}(\text{CO})_2$  moiety, and the fact that we never observe the single band corresponding to the  $\text{Mn}(\text{CO})$  moiety, suggests the simultaneous loss of the two carbonyls contrary to what is expected through a step-by-step loss of one CO and then the second.<sup>37,38</sup> This agrees with the mechanism proposed for the formation of nanostructured materials from solid precursors and suggests that volatile components are easily ejected from the matrix during intermediate steps.

The changes in compound (1) on annealing were also investigated by in situ Raman scattering spectroscopy at several temperatures. As shown in Figure 4a, the characteristic D and G bands of graphite<sup>41–43</sup> ( $1000$ – $1600\text{ cm}^{-1}$ ) are found at all laser

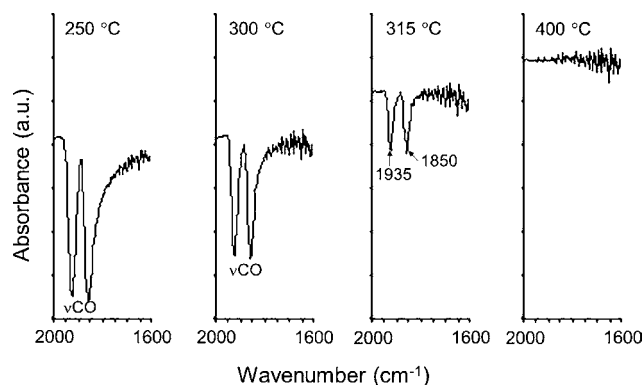


**Figure 3.** FTIR spectra in the wavenumber region  $2000$ – $1600\text{ cm}^{-1}$  from the pyrolytic product from  $\text{NP}(\text{OC}_8\text{H}_{15})_2(\text{OC}_6\text{H}_4\text{PPh}_2\text{-Mn}(\text{CO})_2)(\eta^5\text{-C}_5\text{H}_4\text{Me})_2$  acquired at temperatures in the range  $250$ – $400^\circ\text{C}$ .

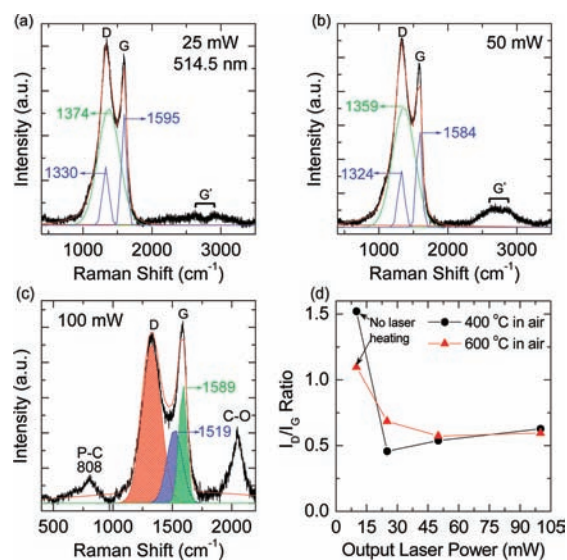


**Figure 4.** (a–c) Raman spectra of the pyrolysis product acquired at a constant temperature of  $400^\circ\text{C}$  at several laser powers. (d)  $I_{\text{D}}/I_{\text{G}}$  ratios for the pyrolytic product as a function laser power acquired at constant temperatures of  $400$  and  $600^\circ\text{C}$ .

power densities (LPD) for a sample that previously underwent constant heating at  $400^\circ\text{C}$ . The D-band is attributed to defects, curved graphite sheets, and lattice distortions in carbon structures, and the G-band is characteristic of graphite.<sup>44–47</sup> Experimental annealing temperatures are calculated from Stokes/anti-Stokes components of the Raman spectra from the peak positions of the Stokes ( $\omega_{\text{S}}$ ) and anti-Stokes ( $\omega_{\text{AS}}$ ) components according to  $n(\omega_{\text{S}})I_{\text{S}} = \{n(\omega_{\text{AS}}) + 1\}I_{\text{AS}}$ , where  $I_{\text{S}}$  and  $I_{\text{AS}}$  are, respectively, the cross sections of the Stokes and anti-Stokes components for each measurement, and  $n(\omega) = 1/\exp(\hbar\omega/k_{\text{B}}T) - 1$  is the Bose-Einstein thermal factor,  $T$  is the sample temperature, and  $k_{\text{B}}$  is Boltzmann's constant. We assume in this case that the thermal conductivity of the carbon acts as a sufficient heat sink so as to maintain a constant temperature at the region of the maximum intensity of the laser beam waist. Cançado et al.<sup>48</sup> have previously shown that 2D graphite is a poorer heat sink than 3D graphite, but the expected downshift in the G band frequency is not observed here.

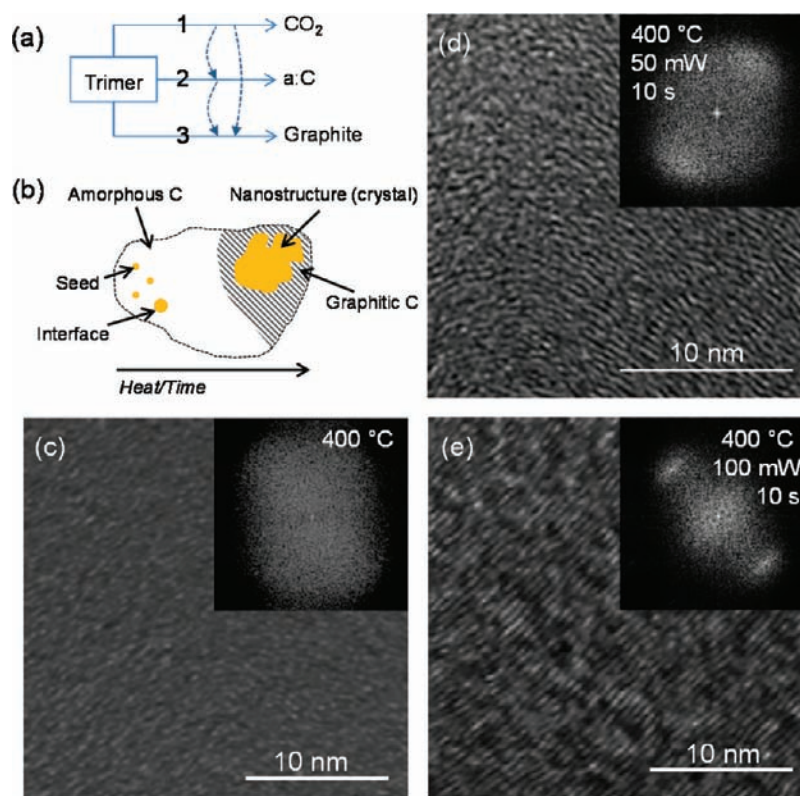


**Figure 5.** Schematic representation of carbon and its graphitization during the pyrolysis of the precursor. (a) Optional paths for the combustion and graphitization of the carbon formed during trimeric decomposition. (b) Nanomaterial seeds and forms within the carbon host with the final nanomaterial lodged within a mostly graphite host material. (c) HRTEM image of the carbon material after pyrolysis at 400 °C and corresponding HRTEM images for pyrolyzed carbon after laser heating at (d) 50 mW for 10 s and (e) layered graphitic carbon after 100 mW irradiation for 10 s.

The observation of the D and G bands in Raman spectra and the fact that both bands are clearly discernible is direct evidence that the decomposition process involves carbonaceous intermediates that contain polycrystalline graphite in a layered form. Deconvolution of other specific spectral bands confirms the presence of P-CH<sub>3</sub> bonds. These organic moieties are typical of an incomplete step in the carbonization of the organic matter, as will be discussed further on. The G band, which usually occurs at  $\sim 1580\text{ cm}^{-1}$  is assigned to a graphite phonon mode often associated with single-layer graphene. The disorder-induced D band (about  $1350\text{ cm}^{-1}$ ) is a phonon associated with lattice defects as it is forbidden in perfect single layers of graphene; the intensity of the D-band has been commonly used for practical applications to evaluate the amount of disorder in carbon materials. In situ heated Raman scattering in Figure 4 shows that the D-band position slightly shifts to lower wavenumbers as excitation power density increases to 25 mW ( $\sim 10^7\text{ W cm}^{-2}$ ).

At 514.5 nm excitation, the G band, associated with graphitic carbon,<sup>49</sup> is located at  $1595\text{ cm}^{-1}$  after initial decarbonylation and decomposition at 400 °C, but prior to locally induced laser power heating. The G-band shows a characteristic single Lorentzian peak, indicative of graphite, as opposed to carbon nanostructures of metallic or semiconducting nature. Additionally, the G-band downshifts in frequency during localized laser induced heating, which confirms the formation of more ordered graphitic sp<sup>2</sup> carbon in the intermediate stages of the trimeric decomposition. In high quality graphite, it is common to observe only the G band. Here, the G band clearly develops with increased local heating. For the D band, one of the two

scattering processes is not phonon-related, but elastic scattering by a defect. Specifically, the G' peak ( $\sim 2700\text{ cm}^{-1}$  at 514.5 nm irradiation) appears as a doublet, which is well-known to result from interlayer coupling in the case of layered carbons and graphite and contributions from 2D and 3D graphite. The G' band corresponds to two-phonon scattering processes where defects are not needed, and is a further confirmation that the resulting carbon intermediate formed during this solid state process is graphitic. In previous studies of polyparaphenylene-based carbon<sup>48</sup> and HOPG, for example, differentiation between 3D and 2D graphite can be obtained from splitting in the G' band. The carbon matrixes contain some 2D and 3D graphite, as seen by HRTEM (Figure 5) for the carbon graphitized during pyrolysis by this method. The main contribution to disorder-induced Raman scattering peaks comes from unaligned 2D graphite. For samples investigated, this misalignment is most profound in curved flakes where even the 2D graphite is disordered.

A characteristic of D and G bands from Raman spectra of graphitic carbons is the ratio of their integrated peak intensities, which gives information on the degree of graphitization of the carbon. The D-band has been used for many years to estimate the graphitic in-plane crystallite size,  $L_a$ , in disordered carbon materials, since the integrated intensity ratio  $I_D/I_G$  is proportional to  $L_a^{-1}$  and also<sup>50,51</sup> to the laser energy,  $E_{\text{laser}}^{-4}$ . We performed measurements using predefined laser powder densities to control localized heating, for precursors pyrolyzed at 400 °C (as for Figure 4a–c) and also after heating at 600 °C. Pyrolysis at 400 °C allowed examination of the carbonized matrix after the removal of CO<sub>2</sub> and CO. During the

decomposition of the precursor, we observe (Figure 4d) that the  $I_D/I_G$  ratio initially follows what is expected for thermal treatment of carbon with a decrease in the ratio (more amorphous carbon, less graphite). In Figure 4d, the  $I_D/I_G$  ratios as a function of laser energy, measured after pyrolysis to 400 and 600 °C, follow a tendency different to that observed in other graphitization processes.<sup>42</sup> Typically, in graphitization processes, the  $I_D/I_G$  ratio decreases with the increasing laser energy, and scales as indicated above, particularly when disorder is introduced into the graphite. In the present case, we observe the decrease of the  $I_D/I_G$  ratio from 10 to 25 mW ( $<10^7$  W cm<sup>-2</sup>), followed by an increase at successively higher laser power densities for samples previously pyrolyzed at 400 and 600 °C. This behavior can be explained with the help of the scheme shown in Figure 5. The initial decrease of  $I_D/I_G$  is interpreted as the carbonization process upon annealing, provoked here by the incident laser radiation after the trimer was pyrolyzed to cleave the metal centers from the precursor and allow crystal growth within the carbon matrix. Under normal combustion conditions, the majority of the organic material is converted to carbon at 600 °C. The slight increase with laser power confirms some disorder within the graphite, and the ultimate graphitic phase is found to be similar after laser heating of carbon formed at 400 and 600 °C; the latter attains the final graphitic phase sooner, as seen in Figure 4d.

Not all of the organic matter is converted to carbon at these temperatures (some P-CH<sub>3</sub> bonds are detected among others), in spite of metal center cleavage and the initiation of inorganic nanomaterial growth within the carbon matrix. Although partially graphitized carbon phonons are observed from the matrix after heating to 400 °C, generation of CO<sub>2</sub> occurs (step 1, Figure 5a), as was detailed using FTIR (Figure 3). As seen in Figure 4c, remnant C–O bonds are detected after laser heating for sample pyrolyzed at 400 °C, and subsequently removed with increased laser power, while the carbon is continually converted to graphite through localized Joule heating from the incident photon energy (Figure 4b and c). After carbonization of organic matter, graphitization occurs continually with time at intermediate temperatures. At successively higher laser powers both graphite formation and organic matter decomposition occurs (steps 2 and 3) with the latter eventually dominating at  $T \sim 800$  °C.

**3.3. Structure and Composition of the Layered Graphitic Host.** When the organic matter decomposes, the initial carbons are amorphous and thus the ratio of amorphous carbon to graphitic carbon in regions where the organic matter has not yet decomposed, will show an decrease in the  $I_D/I_G$  ratio upon raising the temperature by incident light. At 400 and 600 °C (Figure 4d), this process becomes self-limiting; organic matter decomposing to amorphous carbon will subsequently convert to graphite (step 3) at higher temperatures, indicating an equilibrium between organic matter converting to amorphous carbon, and amorphous carbon formed by the initial sample heating, converting to graphite. Specific details of the chemistry in each of these steps is summarized elsewhere,<sup>37,38</sup> and it is likely that the true mechanism involves a complex interplay of all three steps and others not readily identifiable that might be linked to the influence of the mixed 2D and 3D structure of the matrix and the degree of porosity and its uniformity. We investigated the carbon material after pyrolysis at 400 °C using HRTEM. After initial pyrolysis, Figure 5c confirms a mostly amorphous carbon. With laser heating at 50 mW for 10 s (Figure 5d), we observe the

development of turbostratic graphitic layers with some degree of ordering, and this is found the develop to reasonably well ordered, layered graphite after 10 s with 100 mW irradiation, seen in Figure 5e. The fast Fourier transforms confirm layer development. The arcing of the FFT spots in the well-developed graphite is due to imperfect layering and stacking. These measurements directly confirm the Raman scattering and chemical decomposition mechanism whereby the carbon material continually graphitizes. Only a few regions could be found that showed ordered layering; the majority of graphitic carbon consists of a “foam” with varied 2D and 3D layering in well-graphitized areas. It should be noted that this layered carbon disintegrates after 3 min of continued electron beam irradiation at 200 kV.

We have found that pyrolytic products from polymers are sponge-like because of the chain structure of the precursor in the amorphous solid-state matrix; the “walls” of these sponges are composed of quasi-layered graphite. The different morphology from the cyclic derivative (1) reported here confirms that the intermediate matrix formed during heating is crucial for the generation of the pyrolytic materials. Since this matrix is solid, its structure is linked to the precursor structure and decomposition mechanisms. At 800 °C the carbon content, as evident in Figure 2c, reduces to a negligible amount confirming that the organic matter is almost completely eliminated after heating to this temperature. Conversely, the relative atomic percentage of Mn (Figure 6) is reduced

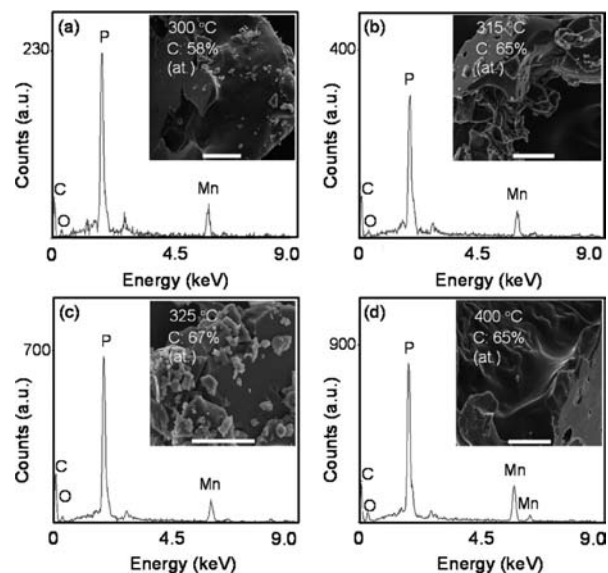


**Figure 6.** EDAX analysis for the pyrolytic product measured after pyrolysis to temperatures in the range 300–400 °C. (Insets) Corresponding SEM images of the C-pyrolytic product in the same temperature range. Scale bar = 70  $\mu$ m.

compared to that of P (cf. Figure 2c) which agrees with the overall formation mechanism: the total quantity of P from the P-containing precursor is being converted to Mn<sub>2</sub>P<sub>2</sub>O<sub>7</sub> while the organic matter is continually combusted.

The formation of carbon during the decarbonylation and subsequent decomposition processes was also monitored using SEM-EDAX analysis. Quantitative determination of the change in the amount of total carbon formed, both amorphous and graphitic, is shown in Figure 6 as a function of temperature. While a graphitization process clearly occurs, it is the

intermediate temperature range (300–600 °C) where the initial decomposition occurs and the final carbon content, type, and structure is found. We characteristically observe the highest C content in the range 300–400 °C. The maximum quantitative C content is found at the same temperature where the complete disappearance of the  $\nu\text{CO}$  bands from the cymantrene groups (Figure 3) occurs, and as mentioned above, where the equilibrium position between organic matter decomposition and graphitization of carbon occurs.

The intermediate carbon formation is also accompanied by several changes in the morphology of the resulting inorganic phase. Although the difference between graphitic and amorphous carbon cannot be determined through FESEM, at temperatures of 400 °C and greater, a significant reduction in the density of small, high surface-to-volume ratio particles is observed. On the basis of the evidence, we suggest that as the carbon matrix is removed at higher temperatures, significant agglomeration and ripening of smaller crystals is now possible.

Additionally, the mechanism is influenced by the presence and formation of a stabilizing carbon, which until now was only proposed based on decomposition chemistry; this work identifies this phase, its formation, and conversion to graphite during pyrolysis. The inorganic products, and nanoparticles as a pertinent example of structures formed using this approach, form at temperatures higher than their melting or boiling temperatures, which is indicative of a carbon-containing host which requires elevated temperatures because of the interfacial thermal conductivity between guest particles and host material. High interfacial thermal conductivity also prevents phase sublimation, allowing structures to form within a decomposing, but stabilizing carbon-containing host material until all that remains (Figure 6) is the final pyrolytic product. Additionally, it has been shown that the rates of  $\text{CO}_2$  evolution (Figure 5a, step 1) can also influence the resulting products formed.<sup>52</sup>

The electronic structure of the carbon matrix after pyrolysis to 600 °C was determined by NEXAFS analysis of the C 1s core level excitations. The measured core edge structure from NEXAFS spectra can be directly correlated to C 1s electronic transitions from the C 1s core level to unoccupied states with  $\pi^*$  ( $1s \rightarrow \pi^*$ ) and  $\sigma^*$  ( $1s \rightarrow \sigma^*$ ) form. Figure 7 compares the NEXAFS spectra of the graphitic carbon material to that of highly oriented pyrolytic graphite (HOPG). The graphitic carbon matrix spectrum shows a smooth edge that is characteristic of a disordered  $\text{sp}^2$ -bonded matrix. The splitting of the C 1s  $\pi^*$  peak in the  $1s \rightarrow \pi^*$  pre-edge region into peaks at 284.5 and 286.2 eV confirms the matrix contains two dissimilar  $\text{sp}^2$  carbons.<sup>53</sup> The lower energy peak corresponds to distorted  $\text{sp}^2$  bonds from a disordered phase. The small feature at 288.7 eV stems from the presence of hydrogen and oxygen functional groups in the carbon consistent with the mechanism proposed and the detection of C–O groups and related from Raman scattering and IR analyses. The graphitic carbon matrix can thus be described as a predominantly  $\text{sp}^2$  hybridized carbon network coexisting with a small quantity of amorphous carbon (distorted  $\text{sp}^2$  bonds). Continued pyrolysis removes remnant  $\text{sp}^3$  phases related to the presence of oxygen.

Our findings are in agreement with those obtained from the formation of Ag nanoparticles from thermal decomposition of silver/acetylenecarboxylic salts.<sup>54</sup> In that case, solid-state pyrolysis of  $\text{Ag}_2(\text{C}_4\text{O}_4)$  at 300 °C leads to the formation of silver nanoparticles embedded in a carbon matrix. HRTEM analysis revealed graphitic layers surrounding the individual Ag nanoparticles. Crystalline graphite has also been observed from

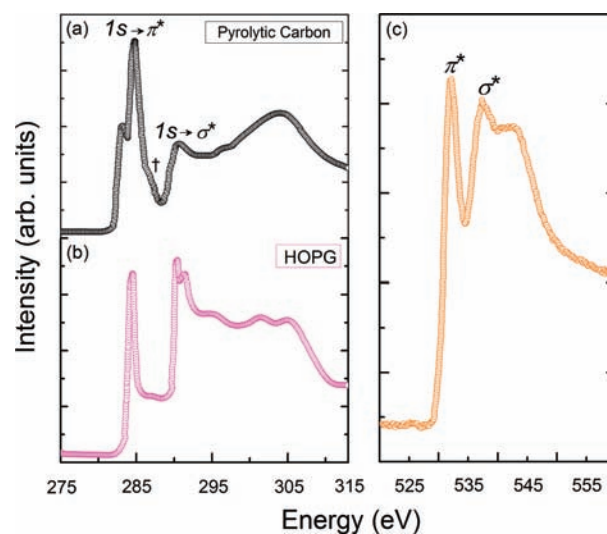


**Figure 7.** (a) NEXAFS spectra of the carbon K-edge from (a) the carbon matrix after pyrolysis and (b) HOPG. (c) Normalized NEXAFS spectrum of the oxygen K-edge from the pyrolytic carbon sample.

solution-based thermal decomposition of  $\text{Fe}(\text{COD})_2$  at 110 °C.<sup>55</sup> This was observed after removal with HCl of the  $\text{Fe}_3\text{O}_4$  nanoparticles that formed.

The direct observation that graphitic carbon forms during this pyrolytic process gives further insight into the application of this new solid state strategy for nanostructure formation of metals, oxides and (pyro)phosphates. While the technique is widely applicable to any valve, noble, and transition metal capable of successful coordination to an appropriate organometallic derivative of poly or cyclophosphazenes, and their mixtures, the control of nanostructure size distribution, nanostructure shape and composition, and so forth, is likely to benefit from rational precursor design to allow cross-linking polymeric chains (from polymeric precursors to give inorganic foams) or cyclomatrix formation (from cyclic oligomeric precursors to give 2D networks of nanoparticles), and dewetting-mediated patterned deposition of the solid state precursors, which is currently under investigation.

The presence of either a carbon or indeed an oxide-based host is important. The composition of the resulting host matrix, be it C or  $\text{P}_4\text{O}_7$ , influences the nucleation and growth of the coordinated species into separate nanoscale objects, or large porous agglomerates. Comparison to the few successful solid state strategies for nanoparticle growth reported by Tannenbaum et al.<sup>56</sup> is that in systems where solid polymers act as the solid state phase, the rate of the formation of the metallic nanoparticles is strongly limited by the mobility, and consequently by the diffusional rates, of the growing particles in accordance with the La Mer mechanism,<sup>57</sup> and various other growth models, including diffusion driven Ostwald ripening. Such mechanisms directly influence particle density and diffusional mobility within porous and host-material systems, and aside from the fact that this is directly dependent on the precursor design, size, molecular weight, viscosity, and so forth, it also relies on the formation of the thermally conductive carbonaceous host material. The solid graphitic matrix also helps to minimize large scale agglomeration; this is provided by the decomposition of the organic matter to carbon and its subsequent conversion to graphite. The ability to also form

relevant tunnel-structure Li-ion battery materials using pyrophosphates (and also oxides) by this ligand free approach has specific advantages. The conductive carbon additive is formed in intimate contact with the active material. The method alleviates some issues with crystal water for sensitive lithium-containing systems and battery materials.

#### 4. CONCLUSIONS

We have presented evidence for the formation of graphitic carbonaceous species during the intermediate annealing stages of a solid-state pyrolytic process involving trimer cyclo-triphosphazenes that result in the formation of nanoparticles. Specifically, for the trimer  $\{NP(OC_8H_{12})_2(OC_6H_4PPh_2-Mn(CO)_2(\eta^5-C_5H_4Me)_2)\}$ , evidence of intermediate carbon and graphite host matrix formation and its decomposition mechanism was confirmed by the observation of the loss of CO from the  $-Mn(CO)_2$  moiety at  $\sim 320$  °C in one step with the resulting  $Mn_2P_2O_7$  formed as a single-crystal material. The findings confirm that the formation of metallic nanoparticles occurs within this intermediate carbon phase. In situ temperature dependent Raman scattering measurements coupled to microscopy and analytical spectroscopy confirm several steps in the combustion process where the macromolecular precursor cleaves coordinated metals centers, undergoes decarbonylation, and forms amorphous carbon, at temperatures up to 400 °C. In-situ Raman scattering, IR and NEXAFS confirmed HRTEM evidence that carbon forms and subsequently graphitizes, with the formation and eventual elimination of C–O, C=O, and other chemical groups. Subsequently, this carbon converts to a thermally conductive polycrystalline graphite matrix in which individual crystals or pyrophosphates can form. The graphitic matrix essentially acts as a solid-state template to form a one-step composite, and its thermal conductivity prevents phase sublimation. This carbon matrix can then be removed if needed by further heating to 800 °C. The identification of graphitic carbon formation is important for the further development of this ligand-free synthetic approach for inorganic nanocrystal growth in the complete absence of liquids or solutions. For important energy storage applications, the ability to form carbon-oxide and carbon-phosphate composites in one step provides a new route to cation intercalation materials for Li-ion, Na-ion, and emerging alternative batteries.

#### AUTHOR INFORMATION

##### Corresponding Author

\*E-mail: cdiaz@uchile.cl (C.D.), c.odwyer@ucc.ie (C.O'D.).

##### Present Address

<sup>⊗</sup>Department of Chemistry, University College Cork, Cork, Ireland, and Tyndall National Institute, Lee Maltings, Cork, Ireland.

##### Notes

The authors declare no competing financial interest.

#### ACKNOWLEDGMENTS

Financial support by FONDECYT (project 1085011) is gratefully acknowledged. Part of this work was conducted under the framework of the INSPIRE program, funded by the Irish Government's Programme for Research in Third Level Institutions, Cycle 4, National Development Plan 2007-2013. This work was also supported by Science Foundation Ireland under contract no. 07/SK/B1232a.

#### REFERENCES

- (1) Iijima, S. *Nature* **1991**, *354*, 56–58.
- (2) Geim, A. K.; Novoselov, K. S. *Nat. Mater.* **2007**, *6*, 183–191.
- (3) Heer, W. A. d.; Chatelain, A.; Ugaarte, D. A. *Science* **1995**, *270*, 1179–1181.
- (4) Nojeh, A.; Lakatos, G. W.; Peng, S.; Cho, K.; Pease, R. F. W. *Nano Lett.* **2003**, *3*, 1469.
- (5) Collions, P. G.; Zettl, A.; Bando, H.; Thess, A.; Smalley, R. E. *Science* **1997**, *278*, 100–102.
- (6) Barros, E. B.; Demir, N. S.; Filho, A. G. S.; Filho, J. M.; Jorio, A.; Dresselhaus, G.; Dresselhaus, M. S. *Phys. Rev. B* **2005**, *71*, 165422.
- (7) Klett, J.; Hardy, R.; Romine, E.; Walls, C.; Burchell, T. *Carbon* **2000**, *38*, 953.
- (8) Dresselhaus, M.; Dresselhaus, G.; Saito, R. *Carbon* **1995**, *33*, 883–891.
- (9) Grobert, N. *Mater. Today* **2007**, *10*, 28–35.
- (10) Rao, C. N. R.; Kulkarni, G. U.; Govindaraj, A.; Satishkumar, B. C.; Thomas, P. J. *Pure Appl. Chem.* **2000**, *72*, 21–33.
- (11) Rao, C. N. R.; Govindaraj, A. *Acc. Chem. Res.* **2002**, *35*, 998–107.
- (12) Liu, Z.; Zhou, X.; Quian, Y. *Adv. Mater.* **2010**, *22*, 1–4.
- (13) Sen, R.; Govindaraj, A.; Rao, C. N. R. *Chem. Mater.* **1997**, *9*, 2078–2081.
- (14) Ma, Y.; Hu, Z.; Huo, K.; Lu, Y.; Hu, Y.; Liu, Y.; Hu, J.; Chen, Y. *Carbon* **2005**, *43*, 1667.
- (15) Turkevich, J. *Gold Bull.* **1985**, *18*, 86–91.
- (16) Brust, M.; Walker, M.; Bethke, D.; Schiffrin, D.; Whyman, R. J. *J. Chem. Soc., Chem. Commun.* **1994**, 801–802.
- (17) Edelstein, A. S.; Cammarata, R. C. *Nanomaterials: Synthesis Properties and Applications*; J. W. Arrowsmith Ltd: Bristol, U.K., 2000.
- (18) Diaz, C.; Valenzuela, M. L. *Metallic Nanostructures Using Oligo and Polyphosphazenes as Template or Stabilizer in Solid State*; American Scientific Publishers: Valencia, CA, 2011.
- (19) Petersen, R.; Foucher, D. A.; Tang, B. Z.; Lough, A.; Raju, N. P.; Greedan, J. E.; Manners, I. *Chem. Mater.* **1995**, *7*, 2045.
- (20) Leite, E. R.; Carreño, N. L. V.; Longo, E.; Pontes, F. M.; Barison, A.; Maniette, Y.; Varela, J. A. *Chem. Mater.* **2002**, *14*, 3722–3729.
- (21) Boxall, D. L.; Kenik, E. A.; Lukehart, C. M. *Chem. Mater.* **2002**, *14*, 1715–1720.
- (22) Wostek, W.; Dorota, J.; Jeszka, K. J.; Amiens, C.; Chaudret, B.; Lecante, P. *J. Colloid Interface Sci.* **2005**, *287*, 107.
- (23) Diaz, C.; Valenzuela, M. L. *J. Inorg. Organomet. Polym. Mater.* **2006**, *16*, 211–218.
- (24) Diaz, C.; Valenzuela, M. L.; Zuñiga, L.; O'Dwyer, C. *J. Inorg. Organomet. Polym. Mater.* **2009**, *19*, 507–520.
- (25) Diaz, C.; Valenzuela, M. L.; Bravo, D.; Lavayen, V.; O'Dwyer, C. *Inorg. Chem.* **2008**, *47*, 11561–11569.
- (26) Diaz, C.; Valenzuela, M. L.; Spodine, E.; Moreno, Y.; Peña, O. J. *Cluster Sci.* **2007**, *18*, 831–844.
- (27) Jimenez, J.; Laguna, A.; Benouazzane, M.; Sanz, J. A.; Diaz, C.; Valenzuela, M. L.; Jones, P. G. *Chem.—Eur. J.* **2009**, *13*, 13509–13520.
- (28) Diaz, C.; Valenzuela, M. L.; Laguna, A.; Lavayen, V.; Jimenez, J.; Power, L.; O'Dwyer, C. *Langmuir* **2010**, *26*, 10223–10233.
- (29) Diaz, C.; Lavayen, V.; O'Dwyer, C. *J. Solid State Chem.* **2010**, *183*, 1595–1603.
- (30) Finney, E. E.; Finke, R. G. *J. Colloid Interface Sci.* **2008**, *317*, 351–374.
- (31) Skrdla, P. J.; Robertson, R. T. *Chem. Mater.* **2008**, *20*, 3.
- (32) Philipe, L.; Michler, J. *Small* **2008**, *4*, 904–907.
- (33) Goia, D. V. *J. Mater. Chem.* **2004**, *14*, 451–458.
- (34) Capek, I. *Adv. Colloid Interface Sci.* **2004**, *110*, 49–74.
- (35) Tadd, E.; Zeno, A.; Zubris, M.; Dan, N.; Tannenbaum, R. *Macromolecules* **2003**, *36*, 6497–6502.
- (36) Hautier, G.; Jain, A.; Ong, S. P.; Kang, B.; Moore, C.; Doe, R.; Ceder, G. *Chem. Mater.* **2011**, *23*, 3495–3508.
- (37) Carriedo, G.; Garcia-Alonso, F. J.; González, P. A.; Diaz, C.; Yutronic, N. *Polyhedron* **2002**, *21*, 2579–2586.



- (38) Diaz, C.; Valenzuela, M. L.; Bravo, D.; Lavayen, V.; O'Dwyer, C. *J. Colloid Interface Sci.* **2011**, *362*, 21–32.
- (39) Díaz, C.; Valenzuela, M. L. *J. Inorg. Organomet. Polym. Mater.* **2006**, *16*, 123–128.
- (40) Diaz, C.; Carriedo, G. A.; Valenzuela, M. L. *Polymer Bull.* **2009**, *63*, 829–835.
- (41) Endo, M.; Nishimura, K.; Kim, Y. A.; Hakamada, K.; Matsushita, T.; Dresselhaus, M. S.; Dresselhaus, G. *J. Mater. Res.* **1999**, *14*, 4474–4477.
- (42) Nemanich, R. J.; Solin, S. A. *Phys. Rev. B* **1979**, *20*, 392–401.
- (43) Campos-Delgado, J.; Farhat, H.; Kim, Y. A.; Reina, A.; Kong, J.; Endo, M.; Muramatsu, H.; Hayashi, T.; Terrones, H.; Terrones, M.; Dresselhaus, M. S. *Small* **2009**, *5*, 2698–2702.
- (44) Tang, C.; Wooley, K. K.; Matyjaszewski, K.; Kowalewski, T. *Angew. Chem., Int. Ed.* **2004**, *43*, 2783–2787.
- (45) Lee, K. T.; Ji, X.; Rault, M.; Nazar, L. *Angew. Chem., Int. Ed.* **2009**, *48*, 1–6.
- (46) Dresselhaus, M. S.; Jorio, A.; Hofmann, M.; Dresselhaus, G.; Saito, R. *Nano Lett.* **2010**, *10*, 751–758.
- (47) Dresselhaus, M. S.; Dresselhaus, G.; Jorio, A.; Filho, A. G. S.; Pimenta, M. A.; Saito, R. *Acc. Chem. Res.* **2002**, *35*, 1070–1078.
- (48) Cancado, L. G.; Pimenta, M. A.; Saito, R.; Jorio, A.; Ladeira, L. O.; Grueneis, A.; Souza-Filho, A. G.; Dresselhaus, G.; Dresselhaus, M. S. *Phys. Rev. B* **2002**, *66*, 035415.
- (49) Ferrari, A. C.; Robertson, J. *Phil. Trans. R. Soc. Lond. A* **2004**, *362*, 2477–2512.
- (50) Tuinstra, F.; Koenig, J. L. *J. Chem. Phys.* **1970**, *53*, 1126–1130.
- (51) Matthews, M. J.; Pimenta, M. A.; Dresselhaus, G.; Dresselhaus, M. S.; Endo, M. *Phys. Rev. B* **1999**, *59*, R6585–R6588. O'Dwyer, C.; Lavayen, V.; Ana, M. A. S.; Benavente, E.; González, G.; Torres, C. M. S. *J. Electrochem. Soc.* **2007**, *154*, K29.
- (52) Park, J.; Joo, J.; Kwon, S. G.; Jang, Y.; Hyeon, T. *Angew. Chem., Int. Ed.* **2007**, *46*, 4630–4660.
- (53) Tang, Y. H.; Zhang, P.; Kim, P. S.; Sham, T. K.; Hu, Y. F.; Sun, X. H.; Wong, N. B.; Fung, M. K.; Zheng, Y. F.; Lee, C. S.; Lee, S. T. *Appl. Phys. Lett.* **2001**, *79*, 3773.
- (54) Dallas, P.; Bourlinos, A. B.; Komninou, P.; Karakassides, M.; Niarachos, D. *Nanoscale Res. Lett.* **2009**, *4*, 1381–1388.
- (55) Walker, E. C.; Beetz, T.; Sfeir, M. Y.; Brus, L. E.; Steigerwald, M. L. *J. Am. Chem. Soc.* **2006**, *128*, 15590–15591.
- (56) Rotstein, H. G.; Novick-Cohen, A.; Tannenbaum, R. *J. Stat. Phys.* **1998**, *90*, 119–143.
- (57) LaMer, V. K.; Dinegar, R. H. *J. Am. Chem. Soc.* **1950**, *72*, 4847–4847.